

# The impact of feedback from galaxy formation on the Lyman- $\alpha$ transmitted flux

Matteo Viel<sup>1,2</sup>, Joop Schaye<sup>3</sup> & C. M. Booth<sup>3,4,5</sup>

<sup>1</sup> *INAF - Osservatorio Astronomico di Trieste, Via G.B. Tiepolo 11, I-34131 Trieste, Italy (viel@oats.inaf.it)*

<sup>2</sup> *INFN/National Institute for Nuclear Physics, Via Valerio 2, I-34127 Trieste, Italy*

<sup>3</sup> *Leiden Observatory, Leiden University, P.O. Box 9513, 2300 RA Leiden, the Netherlands*

<sup>4</sup> *Department of Astronomy and Astrophysics, The University of Chicago, Chicago, IL 60637, USA*

<sup>5</sup> *Kawli Institute for Cosmological Physics and Enrico Fermi Institute, The University of Chicago, Chicago, IL 60637, USA*

4 September 2018

## ABSTRACT

The forest of Lyman- $\alpha$  absorption lines seen in the spectra of distant quasars has become an important probe of the distribution of matter in the Universe. We use large, hydrodynamical simulations from the OWLS project to investigate the effect of feedback from galaxy formation on the probability distribution function and the power spectrum of the Lyman- $\alpha$  transmitted flux. While metal-line cooling is unimportant, both galactic outflows from massive galaxies driven by active galactic nuclei and winds from low-mass galaxies driven by supernovae have a substantial impact on the flux statistics. At redshift  $z = 2.25$ , the effects on the flux statistics are of a similar magnitude as the statistical uncertainties of published data sets. The changes in the flux statistics are not due to differences in the temperature-density relation of the photoionised gas. Instead, they are caused by changes in the density distribution and in the fraction of hot, collisionally ionised gas. It may be possible to disentangle astrophysical and cosmological effects by taking advantage of the fact that they induce different redshift dependencies. In particular, the magnitude of the feedback effects appears to decrease rapidly with increasing redshift. Analyses of Lyman- $\alpha$  forest data from surveys that are currently in process, such as BOSS/SDSS-III and X-Shooter/VLT, must take galactic winds into account.

**Key words:** cosmology: theory – methods: numerical – galaxies: intergalactic medium – quasars: absorption lines

## 1 INTRODUCTION

The H I Lyman- $\alpha$  forest, i.e. the multitude of H I Lyman- $\alpha$  absorption lines seen in the spectra of distant quasars (QSOs), is an important cosmological observable that probes matter density fluctuations in the intergalactic medium (IGM) over a unique range of redshifts, scales and environments. Many attempts have been made to measure physical properties of the IGM using Lyman- $\alpha$  forest data. The two most common approaches are either based on decomposing the information encoded in the transmitted flux via Voigt profile fitting or treating the flux as a continuous field with directly measurable statistical properties (e.g. Rauch 1998; Croft et al. 1998, 2002; Meiksin 2009). In the second approach, measurement of the zero-, one-, two- or three-point probability distribution functions (i.e. the mean flux level, the flux probability distribution function, the flux power and bispectrum) enable a variety of physical properties to be explored. The mean flux level for example, is

sensitive to the amplitude of the meta-galactic Ultra Violet (UV) background (e.g. Rauch et al. 1997; Tytler et al. 2004; Bolton et al. 2005) while the flux probability distribution function (PDF) is sensitive to the thermal evolution of the IGM (e.g. Theuns et al. 2000; McQuinn et al. 2009; Bolton et al. 2009; Peeples et al. 2010b,a). The flux power spectrum has been used to constrain cosmological parameters and the behaviour of dark matter (DM) at small scales (Croft et al. 1999; Viel et al. 2004; Seljak et al. 2006; Viel et al. 2008), the flux bispectrum can be used to search for signatures of non-Gaussianities in the matter distribution (Viel et al. 2009) and wavelet techniques can also be applied in order to constrain the IGM temperature (e.g. Meiksin 2000; Theuns et al. 2002; Garzilli et al. 2012).

The data used for these investigations consist mainly of two sets of QSO spectra: the SDSS low-resolution, low signal-to-noise sample and UVES/VLT or HIRES/KECK samples of high-resolution spectra. The characteristics of the

low- and high-resolution data sets are very different (the number of SDSS spectra is a factor  $\sim 200$  larger than that of high-resolution samples, but the latter probe smaller scales due to the higher spectral resolution). Measurements based on Lyman- $\alpha$  forest data have reached a level of accuracy where an understanding of systematic uncertainties at the percent level or below (the magnitude of statistical errors associated with the SDSS sample) has become important.

In this work we use two sets of simulations to investigate the effects of various physical and cosmological processes on Lyman- $\alpha$  flux statistics. Firstly we use the suite of large cosmological hydrodynamical simulations that comprise the Overwhelmingly Large Simulations project (OWLS; Schaye et al. 2010) to investigate the effect of physical processes such as metal-line cooling and galactic winds driven by supernovae (SNe) and active galactic nuclei (AGN) on the flux statistics. Altay et al. (2011) and Tepper-García et al. (2012) have shown that the OWLS models reproduce the observed H I column density distributions at  $z = 3$  and  $z = 0$ , respectively. Secondly, we use sets of simulations in which cosmological parameters including the neutrino mass (Viel et al. 2010), the thermal history of the IGM (Viel et al. 2009) and the effect of WDM (Viel et al. 2012) are varied.

Throughout, we focus on the effects of these physical processes on two statistics that have been shown to be very constraining: the flux PDF and the flux power spectrum. These statistics have previously been investigated by several authors either in isolation (e.g. McDonald et al. 2000; Jena et al. 2005; Becker et al. 2007; Lidz et al. 2006; Kim et al. 2007; Bolton et al. 2008), or jointly (e.g. Theuns et al. 2000; Meiksin et al. 2001; Zaroubi et al. 2006; Desjacques et al. 2007). We will compare with the present error bars derived from the flux PDF of high-resolution UVES QSO spectra (Kim et al. 2007) and the flux power measured from the SDSS data (McDonald et al. 2006). Note that ongoing surveys such as BOSS/SDSS-III will strongly reduce these statistical error bars.

Previous simulation studies have found the effect of feedback on the Lyman- $\alpha$  forest to be relatively small, because the winds tend to escape into the voids, leaving the filamentary structures responsible for most of the Lyman- $\alpha$  forest nearly intact (e.g. Theuns et al. 2002; Bruscoli et al. 2003; McDonald et al. 2005; Cen et al. 2005; Kollmeier et al. 2006; Bertone & White 2006; Borgani & Viel 2009; Tornatore et al. 2010; Kawata & Rauch 2007; Tepper-García et al. 2012). However, the precision expected from upcoming surveys implies that even small differences may be important. Moreover, previous work has generally considered only relatively weak feedback processes and as a result has suffered from “overcooling”. Inclusion of the strong feedback that appears to be required to reproduce observations may lead to much stronger effects and qualitative differences, as was recently found for the low- $z$  matter power spectrum (van Daalen et al. 2011; Semboloni et al. 2011). Indeed, the OWLS models have already been used to demonstrate that feedback from galaxy formation changes the density profiles of haloes (Duffy et al. 2010) and the matter power spectrum (van Daalen et al. 2011) to a degree that is highly relevant for upcoming weak lensing experiments

(Semboloni et al. 2011). Furthermore, by using a set of hydrodynamic simulations, galactic feedback either in the form of AGN feedback and/or winds has also been shown to affect the properties of Damped Lyman- $\alpha$  systems and metal systems like CIV (e.g. Tescari et al. (2009, 2011); Barai et al. (2012)) and the properties of the intracluster medium (e.g. Fabjan et al. (2010)).

Recently, Chang et al. (2012) argued that plasma instabilities cause ultra-relativistic pairs produced by blazars to dissipate their energy in the IGM and that this process dominates over photo-heating at low densities. Puchwein et al. (2012) demonstrated that this heating mechanism has the potential to significantly affect the observed Lyman- $\alpha$  forest flux statistics. Although we will confine ourselves to more traditional, and more localised, feedback effects, it should be kept in mind that other feedback mechanisms, such as blazar heating, may also be important.

Here we demonstrate that the effects of outflows driven by feedback effects from galaxy formation may already be comparable to the statistical errors of past and current surveys. We find that the effect of feedback decreases rapidly with increasing redshift, which may make it possible to disentangle astrophysical and cosmological effects.

The plan of the paper is as follows: in Section 2 we describe the simulations used and the physics implemented, in Section 3 we compare models that include different feedback processes and we compare the magnitude of the feedback effects to that of changes in the cosmological parameters and in the thermal history of the IGM. Finally, in Section 4 we present a summary and discuss future perspectives.

## 2 SIMULATIONS

In this work we use cosmological smoothed particle hydrodynamics (SPH) simulations of representative volumes of the Universe taken from the OWLS project (Schaye et al. 2010). Gravitational forces and the hydrodynamic equations are solved with an extended version of the parallel PMTree-SPH code GADGET III (last described in Springel 2005). Our simulations assume a  $\Lambda$ CDM cosmology with parameters from the 3-yr Wilkinson Microwave Anisotropy Probe (WMAP) results<sup>1</sup>,  $\Omega_m = 0.238$ ,  $\Omega_\Lambda = 0.762$ ,  $\Omega_b = 0.0418$ ,  $h = 0.73$ ,  $\sigma_8 = 0.74$  and  $n_s = 0.951$ .

In addition to gravity and hydrodynamic forces, the simulations use sub-grid modules to follow the galaxy formation process. The sub-grid modules used in each simulation include the modelling of star formation, SN feedback, the growth of supermassive black holes (BHs) and AGN feedback, radiative cooling and chemodynamics, as described in Schaye & Dalla Vecchia (2008), Dalla Vecchia & Schaye (2008), Booth & Schaye (2009), Wiersma et al. (2009) and Wiersma et al. (2009), respectively.

Table 1 contains a list of the OWLS simulations used in this study. We begin here by describing our fiducial model (*REF*) before discussing the variations in the sub-grid physics used in the other simulations. In the

<sup>1</sup> These parameter values are largely consistent with the WMAP 7-year results (Komatsu et al. 2011), with the main discrepancy being that  $\sigma_8$  is 8%, or  $2.3\sigma$ , lower in the WMAP 3 data than allowed by the WMAP 7 data.

**Table 1.** Summary of the OWLS models used in the present analysis. The simulations that we analyse differ from one another only in terms of the included feedback processes, and only these parameters are noted here. Each simulation contains  $512^3$  particles of both DM and gas. A more complete description of the physics included in each simulation is present in Sec.2. From left-to-right, the columns contain: (1) simulation identifier, (2) Whether the simulation treats AGN feedback, (3) Whether the simulation includes cooling through metal lines, (4) Whether or not the simulation contains SN winds, and for the simulations that do contain SN winds, columns (5) and (6) list the wind mass-loading and wind velocity. The symbols  $\rho$  and  $v_c$  indicate the gas density local to a feedback event and the host halo circular velocity, respectively.

Simulation <sup>(1)</sup>	AGN <sup>(2)</sup>	Z-cooling <sup>(3)</sup>	SN Winds <sup>(4)</sup>	mass-loading <sup>(5)</sup>	wind-velocity <sup>(6)</sup>
<i>REF</i>	×	✓	✓	2	600
<i>AGN</i>	✓	✓	✓	2	600
<i>NOSN_NOZCOOL</i>	×	×	×	–	–
<i>NOZCOOL</i>	×	×	✓	2	600
<i>WDENS</i>	×	✓	✓	$\propto \rho^{-1/3}$	$\propto \rho^{1/6}$
<i>WML1V848</i>	×	✓	✓	1	848
<i>WML4V424</i>	×	✓	✓	4	424
<i>WML8V300</i>	×	✓	✓	8	300
<i>WVCIRC</i>	×	✓	✓	$\propto v_c$	$\propto v_c^{-1}$

**Table 2.** Summary of the simulations used to probe cosmological parameters and the effect of the thermal state of the IGM. Each simulation is compared to a reference  $\Lambda$ CDM simulation, which is identical apart from any differences described in the fourth column. From left-to-right, the columns list: (1) simulation identifier, (2) Comoving box size in Mpc/h, (3) Number of baryonic particles, (4) Brief description of the difference between each simulation and its corresponding reference case.

Simulation <sup>(4)</sup>	Box Size (Mpc/h) <sup>(2)</sup>	$N_{\text{gas}}^{(3)}$	Description <sup>(4)</sup>
<i>WDM</i>	25	$512^3$	Warm dark matter 1keV vs. $\Lambda$ CDM
$\nu$	60	$512^3$	Neutrino mass $\Sigma m_\nu = 0.6$ eV + $\Lambda$ CDM vs. massless neutrinos + $\Lambda$ CDM
$\gamma$	20	$256^3$	$T - \rho$ relation of the IGM has slope $\gamma = 1.6$ vs. $\gamma = 1.3$
$n_s$	20	$256^3$	Spectral index $n_s = 0.95$ vs. $n_s = 0.9$
$\sigma_8$	20	$256^3$	$\sigma_8 = 0.85$ vs. $\sigma_8 = 0.75$

*REF* simulation, radiative cooling and heating are calculated element-by-element by explicitly following the 11 elements H, He, C, N, O, Ne, Mg, Si, S, Ca and Fe in the presence of the Cosmic Microwave Background and the Haardt & Madau (2001) model for the UV/X-ray background radiation from quasars and galaxies, as described in Wiersma et al. (2009), Wiersma et al. (2009).

Star-forming gas is modelled by imposing a polytropic effective equation of state for dense particles ( $n_{\text{H}} > 10^{-1} \text{ cm}^{-3}$ ). These particles feel a pressure  $P \propto \rho^{\gamma_{\text{eff}}}$ , where  $\gamma_{\text{eff}} = 4/3$  is a polytropic index and  $\rho$  is the proper mass density of the gas. Star formation is followed stochastically (Schaye & Dalla Vecchia 2008), with a pressure dependent star formation rate chosen to match the observed relation between star formation surface density and gas surface density Kennicutt (1998).

The *REF* simulation does not include a prescription for BH growth and AGN feedback, but it does treat feedback from SNe. SN feedback is implemented by injecting  $\sim 40\%$  of the energy released by Type II SNe locally as kinetic energy. Each newly formed star particle kicks on average  $\eta = 2$  of its neighbouring gas particles into the wind, isotropically at a velocity of  $v_w = 600$  km/s. These two parameter values were chosen such that the peak in the global star formation history approximately matches the observations (Schaye et al. 2010). Altay et al. (2011) demonstrated that the reference model agrees with the observed  $z = 3$  H I column density distribution over the full 10 orders of magnitude in H I for which it is measured.

The total energy injected into SN-driven winds is proportional to  $\eta v_w^2$ , but we have some freedom in choosing how the energy is distributed between the mass-loading and wind velocity. We therefore analyse an additional three simulations in which the initial wind velocity and mass-loading are scaled such that the total energy output per unit stellar mass is the same as in *REF*, but the distribution across mass-loading and wind velocity is different. These three simulations are termed *WML1V848* ( $\eta = 1$ ,  $v_w = 848$  km/s), *WML4V424* ( $\eta = 4$ ,  $v_w = 424$  km/s), and *WML8V300* ( $\eta = 8$ ,  $v_w = 300$  km/s).

The *WDENS* simulation is the same as the *REF* simulation but in place of using a constant wind velocity ( $v_w$ ) and mass-loading ( $\eta$ ), both parameters depend on the local gas density such that

$$v_w = 600 \text{ km s}^{-1} \left( \frac{n_{\text{H}}}{0.1 \text{ cm}^{-3}} \right)^{1/6}, \quad (1)$$

$$\eta = 2 \left( \frac{v_w}{600 \text{ km s}^{-1}} \right)^{-2}. \quad (2)$$

This ensures that in the densest regions winds are launched with the largest speeds. For gas on the star-forming equation of state, this scaling gives a wind speed that is proportional to the effective local sound speed. Note that the *REF* and *WDENS* models inject the same amount energy per unit stellar mass. The differences in results therefore result solely from how energy is distributed between mass loading and wind velocity.

In addition, we consider a simulation that where the wind velocity and mass-loading scalings match those predicted by models of radiation pressure driven winds (Murray et al. 2005). Other simulations that employ these ‘momentum driven’ wind scalings have been shown to provide a good match to OVI absorption line statistics (Oppenheimer & Davé 2006). In this simulation, *WVCIRC*, the wind velocity and mass-loading are given by

$$v_w = (5/\sqrt{2})v_c \text{ km/s}, \quad (3)$$

and

$$\eta = (150/\sqrt{2})v_c^{-1}, \quad (4)$$

where  $v_c = \sqrt{GM_{\text{vir}}/R_{\text{vir}}}$  is the host halo circular velocity.

We caution that comparisons of our results to the simulations of Oppenheimer & Davé (2006, 2008, 2009) are problematic because these authors varied the parameters of their models between papers (see Schaye et al. 2010, for a discussion of this point), and they temporarily ‘decouple’ wind particles from the hydrodynamical forces, allowing winds to escape from the interstellar medium, which has a large effect on galaxy properties (see Haas et al. in prep. for a discussion of this point).

The *NOSN\_NOZCOOL* simulation is identical to the *REF* simulation except that it does not contain feedback from SNe and that gas cooling rates assume zero metallicity. *NOZCOOL* is the same as *REF* except that all cooling rates are calculated assuming primordial abundances. We can therefore isolate the effects of SN feedback by comparing simulations *NOSN\_NOZCOOL* and *NOZCOOL*.

With the exception of *NOSN\_NOZCOOL*, all of the OWLS simulations analysed here contain a prescription for SN feedback, but the specific choices for the SN mass-loading and wind-velocity affect the range of halo masses in which SN feedback is effective. Prescriptions with high mass-loadings are able to eject a large amount of gas from objects with low star formation rates, we therefore expect that these prescriptions (*WML4V424* and *WML8V300*) will be able to efficiently remove gas from small galaxies at high redshift. These models could potentially have a large impact on the high- $z$  Lyman- $\alpha$  forest as it is precisely the outflows from these objects that have a large enough volume filling factor to account for observations of metal-line absorption and hence to impact the high- $z$  IGM (e.g. Booth et al. 2012).

Prescriptions with high mass-loadings (and correspondingly low wind velocities) are unable to eject gas from high-mass galaxies because the winds are pressure-confined by the ambient interstellar medium (Dalla Vecchia & Schaye 2008) and because low wind velocities result in large thermal losses in the dense interstellar medium of massive galaxies (Dalla Vecchia & Schaye 2012). Models that use a large wind velocity (*WML1V848*) are therefore able to eject gas from galaxies of higher mass. Comparison of these different simulations can therefore inform us how winds escaping from haloes of different masses affect the statistics of the IGM.

Finally, the *AGN* simulation is the same as *REF* except that it includes BH growth and AGN feedback. These two processes are implemented using the method of Booth & Schaye (2009) which is, in turn, a modified version of the method pioneered by Springel et al. (2005). Seed BHs are inserted into the simulation by regularly running a halo finder and placing small BHs ( $m_{\text{seed}} = 10^5 M_\odot$ ) into

every halo with mass  $> 10^{10} M_\odot$  that does not yet contain a BH. These seed BHs then grow both through merging with other BHs and by Eddington-limited gas accretion. Accretion rates in low-density gas ( $n_{\text{H}} < 10^{-1} \text{ cm}^{-3}$ ) are equal to the Bondi-Hoyle rate. In star-forming gas, this accretion rate is boosted by a factor  $(n_{\text{H}}/10^{-1} \text{ cm}^{-3})^2$  to compensate for the lack of a cold, interstellar gas phase and the finite resolution (see Booth & Schaye 2009 for a discussion). For a given accretion rate,  $\dot{m}_{\text{accr}}$ , the BH growth rate is  $\dot{m}_{\text{BH}} = (1 - \epsilon_r)\dot{m}_{\text{accr}}$ , where  $\epsilon_r = 0.1$  is the radiative efficiency of the BH.

The amount of energy available for AGN feedback is then given by  $\dot{E} = \epsilon_f \epsilon_r \dot{m}_{\text{accr}} c^2$ , where  $c$  is the speed of light and  $\epsilon_f$  is a free parameter. Feedback is implemented by allowing the BH to build up a reservoir of accreted energy until it is capable of heating one of its neighbours by a temperature  $\Delta T = 10^8 \text{ K}$ . This energy is then injected thermally into one of the BH’s surrounding gas particles. The parameter  $\epsilon_f = 0.15$  is set by requiring that the *AGN* simulations reproduce the global BH density at  $z = 0$ .

Each of the physics variations was run in boxes of comoving size  $25 h^{-1} \text{ Mpc}$  and  $100 h^{-1} \text{ Mpc}$  and contained  $512^3$  particles of both gas and DM. This corresponds to an initial gas particle mass of  $1.35 \times 10^6 M_\odot/h$  ( $8.7 \times 10^7 M_\odot/h$ ) in the  $25$  ( $100$ )  $h^{-1} \text{ Mpc}$  boxes, respectively. In Appendix A we use a further set of simulations that use smaller box sizes and degraded numerical resolutions to demonstrate that our conclusions are robust with respect to numerical resolution and box size effects.

We note that for all the OWLS models analysed in this paper, the ‘equation-of-state’ (EOS) of the photo-ionised IGM is basically unchanged and results in the same evolution for the parameters  $T_0, \gamma$  that describe it.

In order to compare the effects induced by feedback on the transmitted Lyman- $\alpha$  flux with those produced by cosmological parameters or different thermal histories, we also consider a second set of hydrodynamical simulations. These simulations were also performed with the *GADGET III* code but they include neither metal enrichment nor AGN feedback and they model star formation using a simplified star formation criterion that converts all the gas particles with  $T < 10^5 \text{ K}$  and densities larger than one thousand times the mean density into stars (Viel et al. 2004). This set of simulations is summarised in Table 2. In brief, we consider: i) a warm DM model (WDM) with a 1 keV mass for the DM particle as presented in Viel et al. (2012). This simulation is compared to a corresponding  $\Lambda$ CDM simulation (these two simulations were performed in a  $25$  comoving  $\text{Mpc}/h$  box with  $2 \times 512^3$  DM and gas particles); ii) two simulations that differ only in their choice of spectral index ( $n_s = 0.95$ ) and matter power spectrum amplitude ( $\sigma_8 = 0.75$ ), relative to the corresponding reference simulation ( $n_s = 1$ ,  $\sigma_8 = 0.85$ ). These simulations were performed in boxes of  $20$  comoving  $\text{Mpc}/h$ , and contain  $256^3$  particles of both DM and gas; iii) two  $20$  comoving  $\text{Mpc}/h$ ,  $2 \times 256^3$  simulations in which the thermal history of the IGM has different power-law indices for the temperature-density relation of the low-density photo-ionised gas, namely  $T = T_0(1 + \delta)^{(\gamma-1)}$ , with  $\gamma = 1.3, 1.6$  as in Viel et al. (2009); iv) a simulation of  $60$  comoving  $\text{Mpc}/h$  with  $512^3$  massive neutrinos of total mass  $\Sigma m_\nu = 0.6 \text{ eV}$  and  $512^3$  DM particles compared with a

simulation in which the neutrinos are massless (Viel et al. 2010).

The mass per gas particle is  $1.5 \times 10^6 M_\odot$  for the WDM simulation,  $5.8 \times 10^6 M_\odot$  for the neutrino simulation, and  $6.1 \times 10^6 M_\odot$  for all the other cases. This second set of simulations is not homogeneous, so we will only use it to highlight the relative differences with respect to the matched reference simulation that corresponds to each simulation ( $\sigma_8 = 0.85$ ,  $n_s = 0.95$ ,  $\gamma = 1.3$  and  $\Sigma m_\nu = 0$ ). The resolution of each of these simulations is sufficient to obtain converged results for the Lyman- $\alpha$  PDF at  $z < 3$  (Bolton et al. 2008; Viel et al. 2009; Calura et al. 2012).

### 3 FLUX STATISTICS

In this Section we focus on two different Lyman- $\alpha$  flux statistics that are widely used for cosmological purposes and for constraining the physical state of the IGM: the flux PDF and the flux power spectrum. From each simulation we extract a set of 10000 random lines-of-sight (LOSs) at  $z = 2.25$ ,  $z = 3$  and  $z = 4$  and compute the transmitted flux along each of the LOS in redshift space (unfortunately for the simulations that are not part of OWLS we could only sample 1000 LOSs). The synthetic spectra were convolved with a Gaussian with FWHM  $6.6 \text{ km s}^{-1}$  and rebinned onto pixels of size  $5 \text{ km s}^{-1}$ . We generally report our results in terms of ratios or relative differences with respect to the corresponding reference model at the same resolution, redshift and box size.

In all the plots shown, we have scaled the optical depth of each simulation to reproduce the same mean flux level as measured from observed UVES/VLT high resolution spectra of Kim et al. (2007), namely:  $\tau_{\text{eff}} = 0.0023 \times (1+z)^{3.65}$  and  $\tau_{\text{eff}} = -\ln \langle F \rangle$  (the value  $\langle F \rangle$  is the mean of the transmitted flux calculated using all the pixels of the simulated spectra). This procedure is justified because the intensity of the ionising background radiation is poorly constrained. Note, however, that the original mean fluxes differ usually by less than one percent between the different simulations at all redshifts. In terms of overall scaling factors for the optical depths, the simulations differ by less than 7% (the scaling factors are also very close to one except for the  $z = 4$  outputs).

We do not consider the impact of resolution and noise on our mock quasar spectra because these factors do not alter any of our conclusions with regards to the flux PDF or power spectrum (e.g. Bolton et al. 2008).

#### 3.1 Redshift $z = 2.25$

##### 3.1.1 Comparison of OWLS models

In Figures 1 and 2 we show the effect of AGN feedback on the  $z = 2.25$  flux PDF (left panel) and flux power (right panel) for two different box sizes (100,512) and (25,512) represented by dotted and solid lines, respectively. Figure 1 shows the actual PDF and flux power in the two cases, while in Figure 2 we plot the fractional differences. The blue lines bracket the  $1\sigma$  error bars obtained from the flux PDF measurement at  $z = 2.07$  of Kim et al. (2007) and the flux power spectrum measurement at  $z = 2.2$  of McDonald et al.

(2006). For the flux PDF the agreement between the two simulations is at the 2-3% level. AGN feedback results in an increase of regions with high transmissivity,  $F > 0.5$ , at the expense of low-transmissivity regions. This is due to the fact that, although the simulations share the same  $T - \rho$  density relation for the photo-ionised, low-density IGM, the gas is distributed differently in the  $T - \rho$  plane in the two scenarios, with AGN feedback increasing the amount of low-density gas with  $T > 10^5 \text{ K}$  relative to the REF simulation. In this case the effect induced is comparable to the  $1\sigma$  (statistical) error bars of the measured flux PDF. In terms of flux power, we find a scale-dependent suppression in the AGN case which can reach the 10% level at the largest scales probed and is  $\sim 5\%$  at  $k = 0.6 \text{ h/Mpc}$ . We find that AGN feedback is likely to suppress the flux power at  $z \approx 2$  by a scale-dependent amount which is slightly larger than the  $1\sigma$  statistical error bars at  $k = 0.2 - 0.6 \text{ h/Mpc}$ .

It is important to note that the flux power spectra of the two AGN simulations do not match perfectly due to the large difference in the numerical resolution of the two runs (a factor 64 in the particle mass). Our implementation of BH growth is sensitive to the numerical resolution for BHs with masses similar or smaller than the gas particle mass (Booth & Schaye 2009). While the low-resolution AGN model reproduces optical and X-ray observations of low-redshift groups of galaxies (McCarthy et al. 2010), the same may not be true for the higher-resolution run, which was too expensive computationally to run past  $z = 2$ .

In Figure 3 we show three different effects on Lyman- $\alpha$  flux statistics: the absence of metal cooling (solid green), the presence of more efficient SN-driven galactic winds (dotted black) and the absence of metal cooling and SN feedback (dashed orange). This Figure refers to  $z = 2.25$ . Turning off metal-line cooling has very little effect, but if in addition SN feedback is turned off, then there are substantial differences. The fact that metal-line cooling has little effect in terms of flux properties is expected since the metallicity of the low-density gas that is responsible for the majority of the absorbers is very low (Wiersma et al. 2011). Without metal cooling there is a decrease of power at very small scale, an expected trend since including metal cooling will increase the amount of baryons inside the haloes.

Turning off SN feedback suppresses high-transmissivity ( $F = 0.6 - 0.8$ ) regions, so the effect on the flux PDF is consistent with that of turning off AGN. Increasing the strength of SN-driven winds in dense gas (*WDENS*) has a similar effect on the flux PDF as including AGN feedback. The effects of feedback processes on the flux power are more confusing: turning on SN feedback (i.e. moving from orange, dashed to green, solid) enhances the power on large ( $k < 2 \text{ h/Mpc}$ ) and suppresses it on small scales, which goes in the opposite direction as the effect of turning on AGN (see Fig. 2). Enhancing the strength of winds in dense gas has very little effect on the flux power except on relatively small scales.

The fact that the AGN feedback has a different trend in terms of flux properties when compared to the SN feedback is due to the fact that these two mechanisms have very distinctive behaviours and impact the IGM temperature-density relation in a different way. In Section 3.1.3 we will see that removing the contribution of gas with  $T > 10^5 \text{ K}$  to the absorption can result in changes that are comparable or larger to those shown by the different feedback models. It

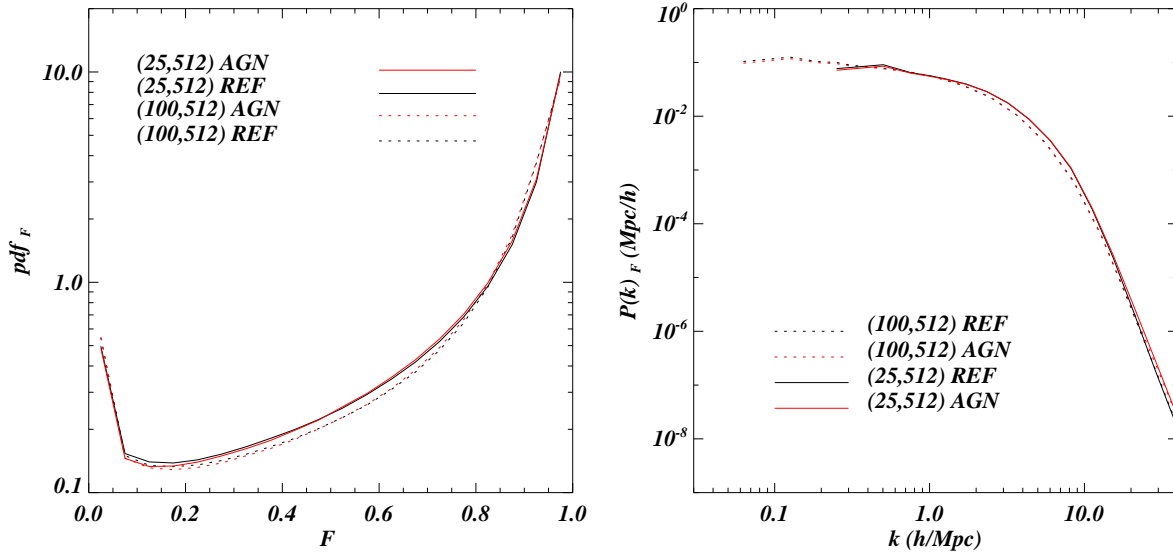


**Figure 1.** Flux PDF (left) and flux power (right) for two different cosmological boxes (100,512 and (25,512) represented by the dotted and solid lines, respectively. We plot the flux PDF and flux power for the AGN (red curves) and REF (black curves) simulations at  $z = 2.25$ .

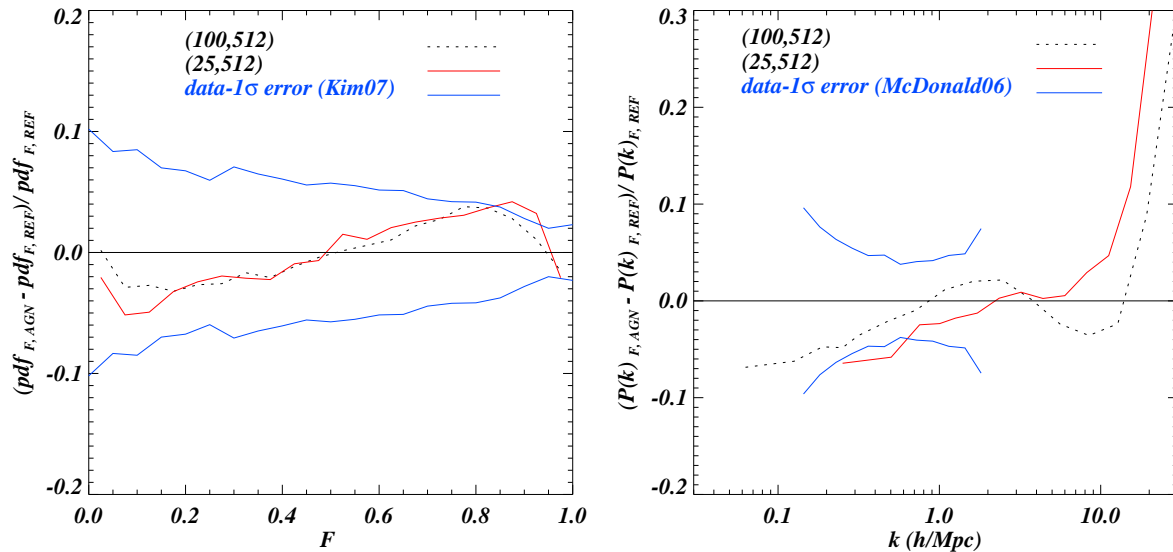


**Figure 2.** Effect of AGN feedback on the flux PDF (left) and flux power (right) for two different cosmological boxes (100,512 and (25,512) represented by the black, dotted and red, solid lines, respectively. We plot the fractional differences between the flux PDF and flux power of the AGN and REF simulations at  $z = 2.25$ . The blue, solid lines bracket the  $1\sigma$  statistical observed errors from UVES/VLT at  $z = 2.07$  PDF (Kim et al. 2007) and SDSS flux power at  $z = 2.2$  (McDonald et al. 2006).

is therefore likely that the difference between SN and AGN feedback is due to thermal and physical differences of the IGM.

In Figure 4 we plot the fractional differences between REF and the three different wind models *WML1V848*, *WML4V424*, *WML8V300* and *WVCIRC* in terms of the flux PDF (left) and flux power (right) at  $z = 2.25$ . For the flux PDF the trends are consistent with

the ones shown in Figures 2 and 3: increasing the efficiency of feedback in higher-mass galaxies (i.e. using higher wind velocities) increases the fraction of high-transmissivity regions at the expense of the low-transmissivity regions. For the flux power the trend is consistent with that of Fig. 3: more efficient winds decrease the power on small scales, but enhance it on the larger scales. As noted above, this is qual-

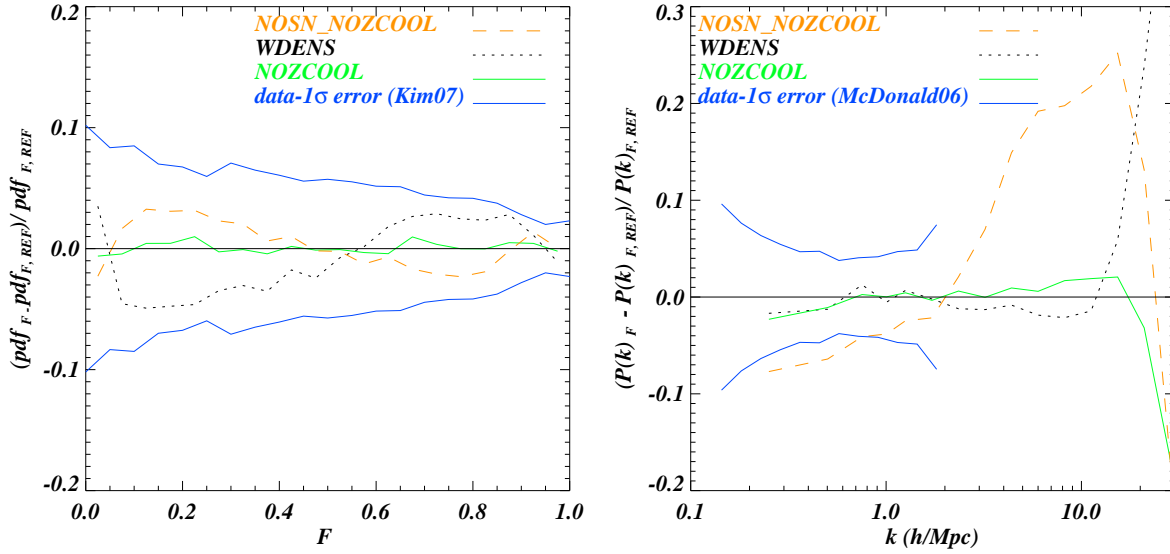


**Figure 3.** Effect of metal cooling, SN feedback and galactic winds in terms of flux PDF (left) and flux power (right) for the (25,512) simulations at  $z = 2.25$ . We plot the fractional differences between the flux PDF and flux power of the *REF* simulation and the following ones: without SN feedback and with primordial cooling (green, solid), with strong SN feedback (black, dotted), with SN feedback and with primordial cooling (orange, dashed). The blue, solid lines bracket the  $1\sigma$  statistical observed errors from UVES/VLT at  $z = 2.07$  PDF (Kim et al. 2007) and SDSS flux power at  $z = 2.2$  (McDonald et al. 2006).

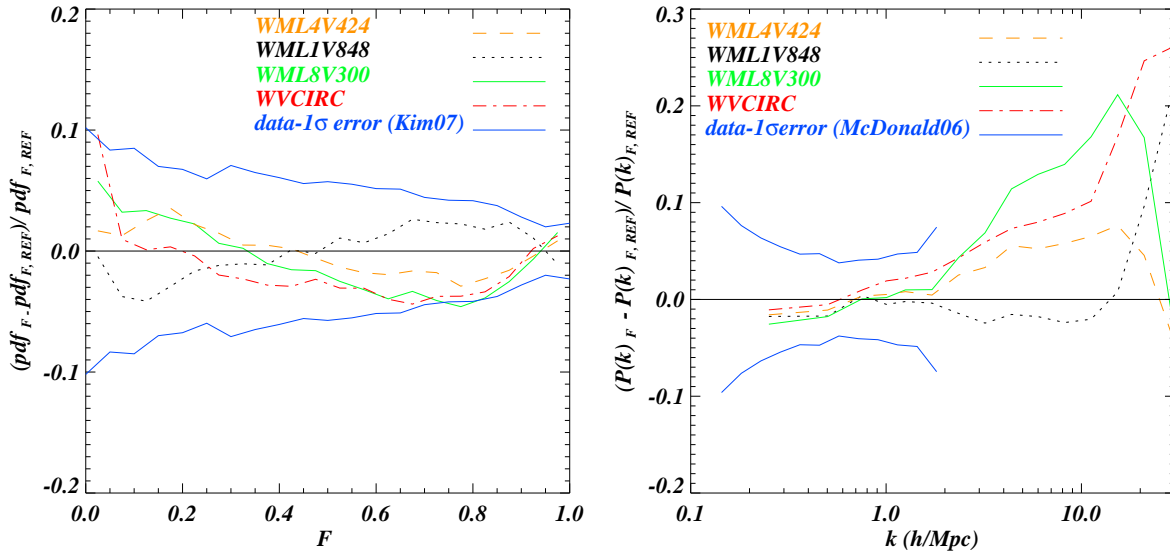


**Figure 4.** Effect of different galactic wind prescriptions in terms of flux PDF (left) and flux power (right) for the (25,512) simulations at  $z = 2.25$ . We plot the fractional differences between the flux PDF and flux power of the *REF* simulation and the following ones: *WML8V300* (green, solid), *WML1V848* (black, dotted), *WML4V424* (orange, dashed curve), *WVCIRC* (red, dot-dashed curve). The blue, solid lines bracket the  $1\sigma$  statistical observed errors from UVES/VLT at  $z = 2.07$  PDF (Kim et al. 2007) and SDSS flux power at  $z = 2.2$  (McDonald et al. 2006).

itatively different from the effect of AGN feedback, which suppresses the power on large scales (see Figure 2).

We note that there is an increasing amount of power at  $k > 1$  h/Mpc when the mass loading of the winds increases (and the wind velocity decreases): redistributing the

gas outside galactic haloes has the effect of producing a larger amount of cold gas (detectable in absorption) at galactic scales that will result in larger amount of power. In the *WML8V300* and *WML4V424* models more gas is moved, increasing the power on small scales. In terms of flux PDF

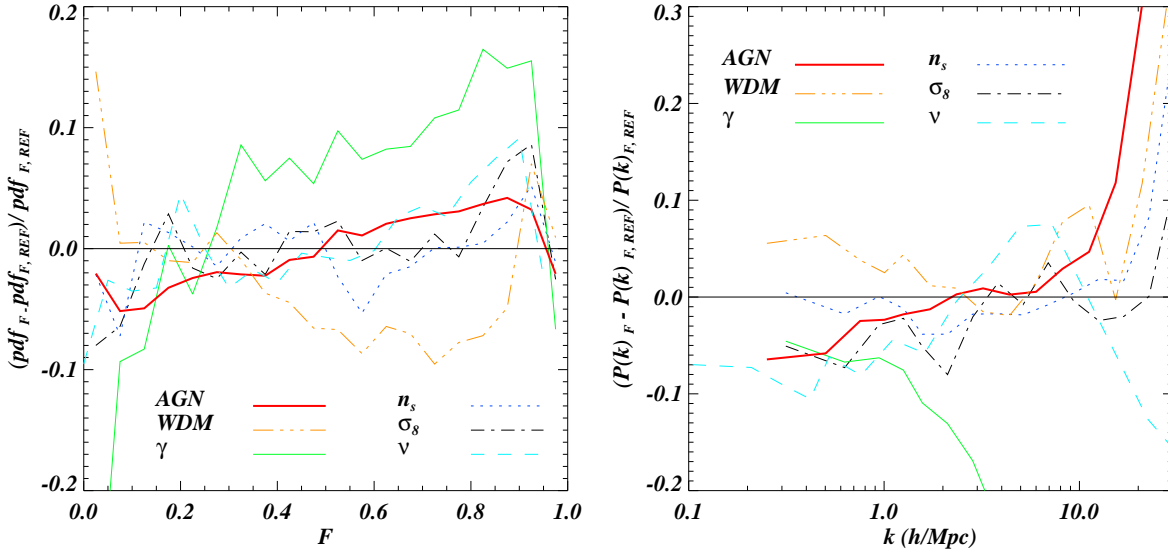


**Figure 5.** Effect of cosmological parameters and thermal state of the IGM on the  $z = 2.25$  flux PDF (left) and flux power (right) compared to the AGN effect (fractional differences are shown). We show the effect of having: a lower  $\sigma_8$  value ( $\sigma_8 = 0.75$ ) compared to the reference case  $\sigma_8 = 0.85$  (black dash-dotted); a lower  $n_s$  value ( $n_s=0.9$ ) compared to the reference  $n_s=0.95$  value (blue, dotted); a higher  $\gamma$  value ( $\gamma = 1.6$ ) compared to the reference  $\gamma = 1.3$  value (green, solid); a thermal WDM relic of 1 keV compared to the  $\Lambda$ CDM case (orange, dash-triple-dotted); a neutrino simulation with  $\Sigma m_\nu = 0.6$  eV (cyan, dashed) and including AGN feedback (red, thick solid). See the text for a more complete description of the simulations used.

these trends (for kinetic driven winds) are similar to those described in (Bolton et al. 2008).

### 3.1.2 Other simulations

In Figure 5 we compare the effect of AGN feedback to effects induced by changing some cosmological and astrophysical parameters. In this latter case, we use published results that have been obtained from other sets of simulations. However, even for these cosmological and astrophysical parameters we compare with a reference case which is reasonably close to the OWLS *REF* simulation. We can see that at  $z \approx 2$  the effect of AGN feedback on the flux PDF is comparable to reducing the value of  $\sigma_8$  by 0.1 and that is larger than decreasing  $n_s$  by 0.05. Changing  $\gamma$ , the power-law index of the temperature-density relation  $T = T_0(1 + \delta)^{\gamma-1}$ , from 1.3 to 1.6, or using a WDM matter power spectrum with thermal  $m_{WDM} = 1$  keV particles, produces effects that are larger than that of the feedback and for the case of WDM they are also of opposite sign.

It is also interesting to compare these models in terms of the flux power (right panel): the effect of including AGN feedback is quite scale dependent, at least at scales  $k < 1h/Mpc$ , while the other effects could be modelled as an overall suppression or increase of power. The magnitude of the AGN feedback effect at the largest scales is comparable to that induced by a different thermal history and that produced by a WDM relic. The neutrino induced suppression of the flux power is of the order of 7-8% on the largest scales (note, however, that the neutrino suppression is computed in a model in which the r.m.s. amplitude of the matter power is normalised at the cosmic microwave background scale).

All the effects not related to the OWLS simulations have been discussed in previous work: for example the effect of neutrinos, is to suppress the growth of structure (and the flux power) and thus to produce a less skewed flux PDF, mimicking a universe with a lower  $\sigma_8$  (Viel et al. 2010); the effect of WDM in terms of flux power is addressed in (Seljak et al. 2006; Viel et al. 2008), where the fact that it can increase the flux power at the largest scales is also shown; the effect of temperature and that of the cosmological parameters with their redshift evolution is instead addressed in (McDonald et al. 2005; Viel & Haehnelt 2006) by using two different hydrodynamic codes.

### 3.1.3 Keeping the temperature-density relation fixed

The differences in the flux statistics between simulations using different feedback prescriptions could be the result of changes in the distribution of the gas density, changes in the ratio of photo-ionised and collisionally ionised gas (i.e. the fraction of the gas with  $T \gg 10^5$  K), or it could be due to changes in the  $T - \rho$  relation of the photo-ionised gas. As the latter relation can be measured from the widths of the absorption lines (e.g. Schaye et al. 1999), it is important to check the role of changes in the thermal state of the diffuse, photo-ionised gas. Below we will follow convention and refer to the  $T - \rho$  relation of the photo-ionised as the “equation of state” (EOS), even though the true equation of state is that of an ideal gas.

We re-analysed a number of simulations after imposing the same EOS in a number of different ways. In each case, the EOS is imposed *a-posteriori* by changing the temperatures of (a subset) of particles and the ionization fractions

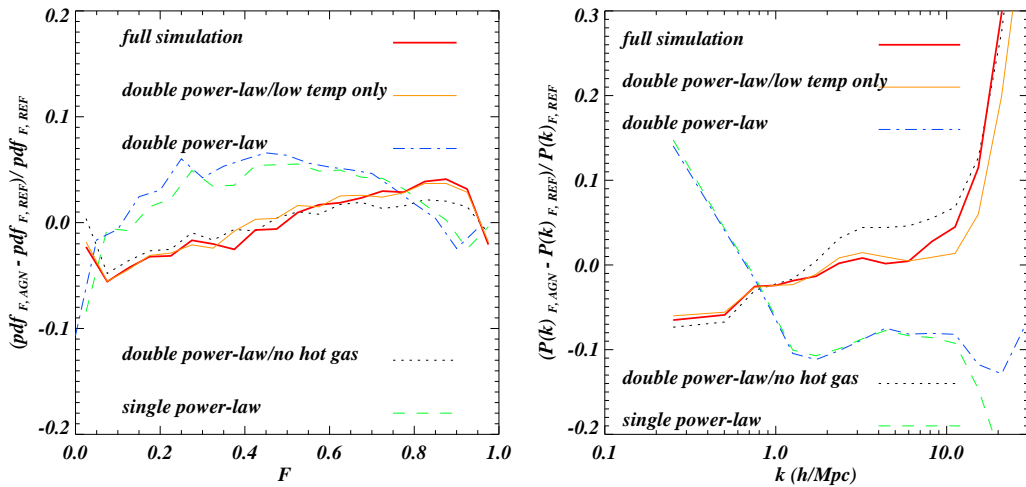


**Figure 6.** Comparison between the *AGN* and *REF* runs at  $z = 2.25$  after imposing an identical  $T - \rho$  relation (EOS) on the gas in the two models. The red thick curve refers to the standard case in which no temperature rescaling is performed (“full simulation”); “single power-law” refers to a case in which all the gas is placed on the EOS that is appropriate for the low-density, photo-ionised IGM (green, dashed curve); “double power-law” refers to a case in which two different EOS are used for the gas below and above an overdensity of  $\delta = 20$  (blue, dot-dashed curve); “double power-law/low-temp only” refers to a case in which gas with  $T > 10^5$  K is left unchanged and lower temperature gas is placed on a double power-law EOS with separate slopes for gas with densities above and below  $10^{-4}$   $\text{cm}^{-3}$  ( $\delta = 20$ ) (orange, continuous curve); “double power-law/no hot gas” refers to the same case as “double power-law” except that the HI fraction of gas with  $T > 10^5$  K is set to zero (black dotted curve).

and spectra are then recalculated. As before, the optical depths are re-scaled so that the mean flux decrement agrees with the observations of Kim et al. (2007) for all models. We consider four different cases:

- **Full simulation:** the thermal state of the gas predicted by the simulation is used, i.e. no EOS is imposed (red curve, Figure 6).

- **Single power-law:** an EOS of the form  $T = T_0(1 + \delta)^{(\gamma-1)}$  is imposed on all gas at all densities, with parameters  $T_0 = 10^{4.66}$  K and  $\gamma = 1.4$  (green, dashed curve in Fig. 6). This EOS fits the  $\rho - T$  relation in the low-density IGM, but overpredicts the temperatures at high density, where radiative cooling is more important than the adiabatic cooling due to the Hubble expansion. We include this case because a single power-law is a common theoretical assumption.

- **Double power-law:** At low densities ( $\delta < 20$ ) the EOS is the same as described above. At high densities ( $\delta > 20$ ), the EOS has a slope of  $\gamma = 0.8$ . This double power-law EOS provides a good fit to the  $T - \rho$  relation of the photo-ionised gas in the simulations and also of the gas at large densities (blue dot-dashed curve in Fig. 6).

- **Double power-law/low-temp only:** gas at high temperatures ( $T > 10^5$  K; this gas is mostly collisionally ionised) retains its original thermodynamic state. At low temperatures, all gas is placed onto an EOS. At low densities ( $\delta < 20$ ) the EOS is the same as described above. At high densities ( $\delta > 20$ ), the EOS has a slope of  $\gamma = 0.8$ . This double power-law EOS provides a good fit to the  $T - \rho$  relation of the photo-ionised gas in the simulations (orange continuous curve in Fig. 6).

- **Double power-law/no hot gas:** this model is the same as the one described directly above, but the density of the hot gas ( $T > 10^5$  K) is set to zero so that it does not

contribute to the absorption (black dotted curve in Fig.6). This allows us to check the effect of absorption by hot gas.

In Figure 6 we show the fractional differences in the flux PDF and the flux power between the  $z = 2.25$  outputs of the *AGN* and *REF* runs, after both simulations have each of the EOSs described above imposed. Note that the red, solid curve (“full simulation”) is identical to the one shown in Figure 2.

We can note the following trends. If we impose a “single power-law” EOS, then the difference between the *AGN* and *REF* models is completely different than if we use the predicted temperatures (“full simulation”). This is because a single power-law strongly overpredicts the temperature of high-density gas, which now becomes collisionally ionised and hence mostly invisible in HI. Moreover, the hot, collisionally ionised low-density gas is now given a low temperature, which increases its HI fraction. Clearly, imposing a single power-law EOS on all gas results in large changes to the flux statistics.

The agreement with the “full simulation” is, however, very good if we use the “double power-law/low-temp only” EOS that results in colder temperature for the high-density gas and which leaves the gas with  $T > 10^5$  K unchanged. Imposing this EOS hardly changes the difference between the *AGN* and *REF* models. The situation is very different if we impose the double power-law EOS also on gas that originally had a temperature  $T > 10^5$  K (dot-dashed blue curve). In this case the result is more similar to the “single power-law” model than to the “double power-law/low-temp only” model.

We can draw two important conclusions from these tests. First, the differences in the flux statistics between the *AGN* and *REF* simulations is not due to changes in the EOS

of the photo-ionised gas, because the difference between the two models is nearly identical if we impose the same, realistic EOS on both simulations. Second, the difference between models *AGN* and *REF* is not only caused by changes in the density distribution, because we obtain completely different results if we impose the double power-law EOS also on gas with  $T > 10^5$  K. The fact that AGN feedback heats gas to temperatures sufficiently high for the gas to become highly collisionally ionised is very important.

Finally, we note that the gas with  $T > 10^5$  K is not completely invisible in HI. We can see this by comparing the cases “double power-law; low-temp only” and “double power-law/no hot gas”. The differences are always below the 4% level in terms of both flux power and flux PDF and of the order of 1-2% at the wavenumbers considered in the SDSS flux power analysis. Thus, excluding the hot gas at temperatures above  $10^5$  K has a small but non-negligible impact on the flux statistics.

### 3.2 Evolution

Up till now we have focused on redshift  $z = 2.25$ , but the flux statistics have been measured over a substantial redshift range. At present, PDF measurements span the redshift range  $z = 2 - 6$  (e.g. Becker et al. 2007) and flux power measurements cover the range  $z = 2.1 - 4.4$  (Croft et al. 2002; Viel et al. 2004; McDonald et al. 2006). The large redshift range may allow one to lift the degeneracies between cosmological and astrophysical parameters and results in tight constraints on the recovered parameters. In this section we will therefore investigate the evolution of the impact of the physical effects by comparing predictions for  $z = 3, 4$  with the results for  $z = 2.25$  that we already showed in the previous sections.

We caution that the predictions for  $z = 3$  and especially for  $z = 4$  are probably not fully converged with respect to the numerical resolution, except for the flux power on large scales (see Appendix A). As we will limit ourselves to comparing different physical models *at the same resolution*, even predictions that are not fully converged are informative. However, we must keep in mind that the comparisons may be affected by the lack of convergence. In particular, the impact of winds driven by low-mass galaxies may well be underestimated when the star formation rate in these objects is limited by the finite resolution of the simulation.

In Figure 7 we compare the *AGN* and the *REF* simulations at  $z = 2.25, 3$ , and 4. The induced suppression of the flux power is 3% smaller at  $z = 3$  than at  $z = 2.25$ , while at  $z = 4$  the models agree since AGN activity, which is restricted to relatively massive galaxies in our *AGN* simulation, is rare at such high redshifts. At high redshift there is a substantial difference in the flux PDF for very high transmissivity regions ( $F > 0.85$ ), but this would be difficult to observe due to continuum fitting errors.

We investigate the redshift dependence of the impact of SN feedback, for the subgrid recipe employed by the *REF* simulation, by comparing the *NOZCOOL* and the *NOSN\_NOZCOOL* models at  $z = 2.25, 3$ , and 4 in Figure 8. On large scales,  $k < 2h/\text{Mpc}$ , the effect on the flux power is nearly identical at  $z = 2.25$  and 3 and at  $z = 4$  the difference between the two models is less than 2%. On smaller scales the evolution is stronger. Interestingly, by  $z = 4$  the effect of

SN feedback only exceeds 2% for  $k > 10h/\text{Mpc}$ . The impact of SN feedback on the flux PDF actually increases with redshift for very high transmissivity regions ( $F > 0.85$ ), but as noted before, continuum fitting errors, which also increase with redshift, in any case limit the usefulness of such regions.

Figure 9 shows the evolution of the difference between simulations *WML8V300* and *REF*. This comparison is interesting, because for low-mass galaxies the winds in model *WML8V300* are more efficient than for *REF*. This is opposite to *AGN*, because AGN feedback only drives strong outflows in massive galaxies. Nevertheless, by  $z = 4$  the difference between *WML8V300* and *REF* is below 2% for both the flux PDF and the flux power, except again for the frequency of very high transmissivity regions and the power on small scales. The *WDENS* simulation (not shown) has instead very little dependence on redshift in terms of flux power. The evolution for *WVCIRC* is weaker than for the *WML8V300* model.

We conclude that the three different feedback scenarios have distinct signatures in the  $(k, z)$  parameter space and that the feedback effects become weaker with increasing redshift, except for the flux PDF in high transmissivity regions. Although many of the feedback effects are too weak to be constrained by present data sets, it will be important to consider them properly when the statistical error bars are reduced further, as will be the case for ongoing surveys such as BOSS/SDSS-III.

## 4 CONCLUSIONS AND DISCUSSION

In this paper we have investigated the effect of feedback from galaxy formation on two widely used Lyman- $\alpha$  flux statistics: the PDF and the power spectrum of the normalised flux. We have used state-of-the-art hydrodynamical simulations from the OWLS project that incorporate most of the physical processes that may affect the properties of the IGM. The suite of OWLS runs, of which we have used only a subset, is particularly well suited for our purposes as the OWLS project was designed to test the effect of uncertain (subgrid) processes by varying one parameter at a time in simulations that start from identical initial conditions.

The impact of feedback on Lyman- $\alpha$  statistics is generically small because galactic winds tend to escape into the voids, leaving the filaments responsible for the Lyman- $\alpha$  absorption largely intact (Theuns et al. 2002). Indeed, Tepper-García et al. (2012) demonstrated this to be true for the OWLS models by comparing the statistics of Voigt profile decompositions of synthetic spectra at low redshift. However, even small differences may be important as the statistical errors on published data, such as the flux PDF measured from high-resolution UVES QSO spectra (Kim et al. 2007) and the flux power measured from the SDSS data (McDonald et al. 2006), are already as small as 5%. Moreover, upcoming observational campaigns such as the BOSS/SDSS-III Lyman- $\alpha$  survey (Eisenstein et al. 2011; Slosar et al. 2011) and the X-Shooter/VLT medium resolution spectrograph (Vernet et al. 2011) are expected to reduce these error bars substantially.

We investigated the effect of metal-line cooling, a number of different implementations of outflows driven by feedback from star formation, and AGN feedback by comparing

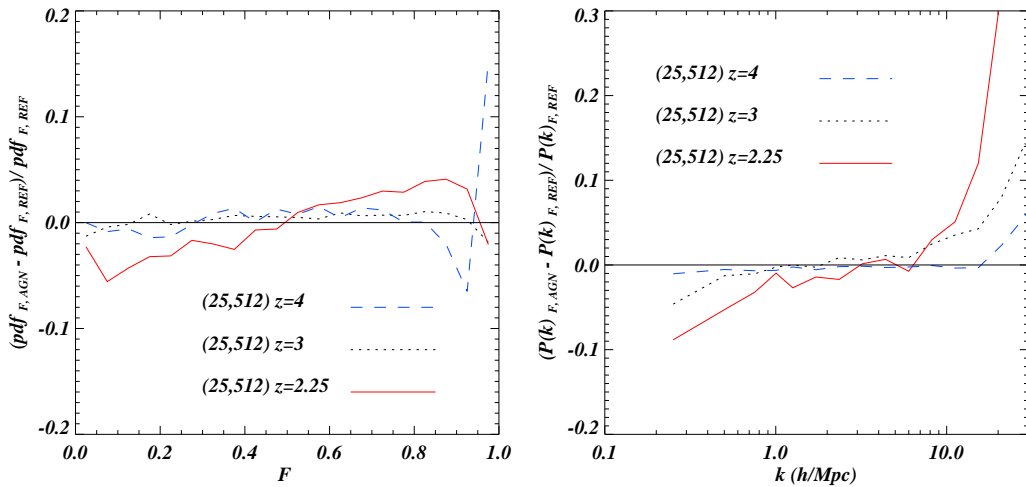


**Figure 7.** Comparison of the effect of AGN feedback on the flux PDF (left) and flux power (right) at redshifts  $z = 2.25$  (solid, red),  $z = 3$  (dotted, black), and  $z = 4$  (dashed, blue). Except for the frequency of very high transmissivity regions, the effect of AGN feedback decreases with redshift.

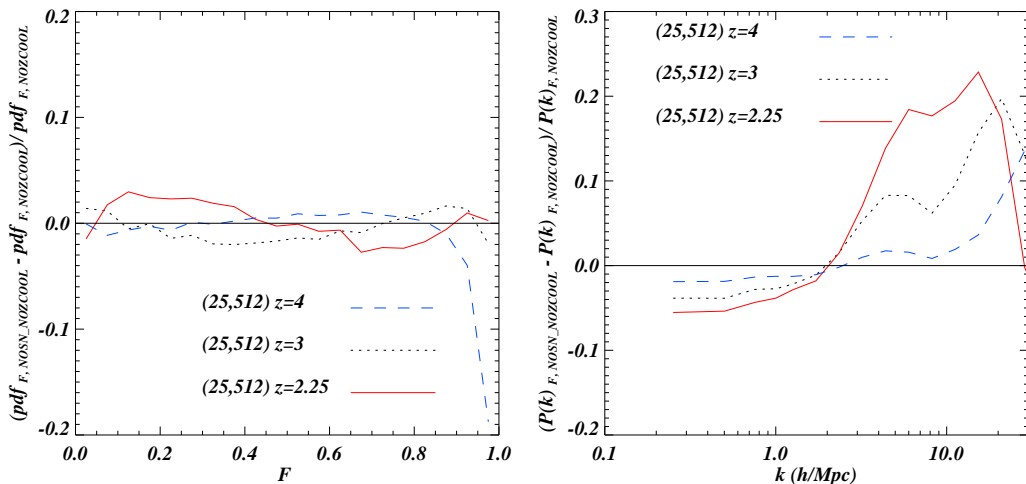


**Figure 8.** Comparison of the effect of SN feedback, using the subgrid recipe employed by the *REF* model, on the flux PDF (left) and flux power (right) at redshifts  $z = 2.25$  (solid, red),  $z = 3$  (dotted, black), and  $z = 4$  (dashed, blue). Except for the frequency of very high transmissivity regions, the effect of SN feedback decreases with redshift.

different OWLS models to the OWLS reference simulation (*REF*). For each redshift the spectra drawn from each simulation were re-scaled to the same, observed mean flux, thus removing a potential source of differences between the models (this procedure is justified because the intensity of the ionising background radiation is poorly constrained). We focused on redshift  $z = 2.25$  but also studied the evolution from  $z = 4$ .

Our main conclusions can be summarised as follows:

- Metal-line cooling has a much smaller effect on the flux statistics than galactic outflows.
- AGN feedback suppresses the flux power on large scales ( $k < 1 h/Mpc$ ). The effect increases in strength with decreasing wave number. At  $z = 2.25$  it reaches  $\sim 10\%$  on the

largest scales we can measure ( $k \sim 0.1 h/Mpc$ ). The flux PDF is changed at the 5% level at this redshift.

- When using the implementation of *REF*, winds driven by SNe have an effect that is qualitatively opposite to that of AGN feedback. The changes in the PDF and the flux power spectrum caused by SN feedback are slightly smaller than for AGN feedback.

- More efficient, but energetically feasible, winds from low-mass galaxies have a strong impact on the flux statistics. At  $z = 2.25$  the effect is similar, both qualitatively and quantitatively, as that of AGN feedback. At higher redshift the impact of such winds changes and is larger than that of AGN feedback.

- Overall, the effects induced by feedback from AGN and

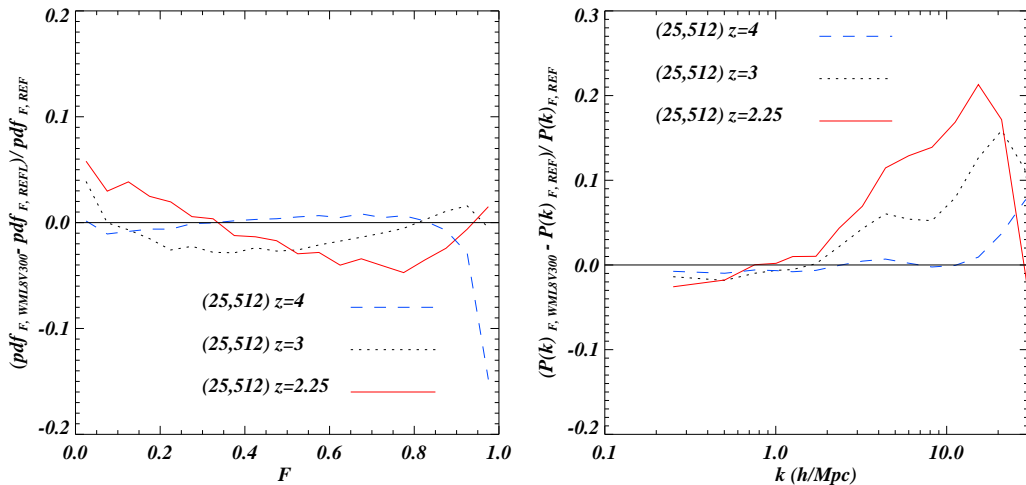


**Figure 9.** Comparison of the difference in the flux PDF (left) and flux power (right) predicted by simulation *WML8V300* and *REF* at redshifts  $z = 2.25$  (solid, red),  $z = 3$  (dotted, black), and  $z = 4$  (dashed, blue). Compared with *REF*, the prescription for SN feedback employed by model *WML8V300* results in stronger outflows in low-mass galaxies. Except for the frequency of very high transmissivity regions, the difference between the flux statistics predicted by the two simulations decreases with redshift.

star formation are of the order of the present  $1\sigma$  statistical error bars, comparable to those induced by cosmological and other astrophysical parameters.

- All the feedback mechanisms studied here have a substantially smaller impact on the Lyman- $\alpha$  forest at higher redshift. For winds from low-mass galaxies we can, however, not rule out that the evolution would be weaker for higher resolution simulations.

- The feedback effects are not due to changes in the temperature-density relation of the diffuse, photo-ionised gas. Instead, they are due to changes in the density distribution of the gas and to changes in the fraction of hot, collisionally ionised gas at a fixed density.

We have shown that the effects of feedback from galaxy formation on Lyman- $\alpha$  flux statistics are not negligible. In particular, at  $z = 2.25$  they are comparable to present observed statistical uncertainties. As upcoming surveys will strongly reduce these statistical errors, it will become necessary to properly account for these effects in future analyses of Lyman- $\alpha$  forest data sets. Although winds driven by feedback from AGN and star formation are difficult to model from first principles, progress can be made by using the fact that their effect on the Lyman- $\alpha$  forest properties could generically have a different scale and redshift dependence than changes in the cosmological model. Further progress in this field can be made by a study at higher resolution and by a more quantitative analysis of the effects discussed here as a function of redshift and scale.

## ACKNOWLEDGMENTS.

We would like to thank all the members of the OWLS team for their contributions to this project. The simulations presented here were run on Stella, the LOFAR BlueGene/L system in Groningen, on the Cosmology Machine at the Institute for Computational Cosmology in Durham as part

of the Virgo Consortium research programme, and on Darwin in Cambridge. This work was sponsored by the National Computing Facilities Foundation (NCF) for the use of supercomputer facilities, with financial support from the Netherlands Organization for Scientific Research (NWO), also through a VIDI grant, and from the Marie Curie Initial Training Network CosmoComp (PITN-GA-2009-238356). MV is supported by ASI/AAE, INFN/PD51, PRIN-INAF, PRIN-MIUR and ERC-StG “cosmoIGM” grants. This research is also supported by the European Research Council under the European Union’s Seventh Framework Programme (FP7/2007-2013) / ERC Grant agreement 278594-GasAroundGalaxies and 257670-cosmoIGM. The authors wish to thank the anonymous referee for the very useful report.

## REFERENCES

- Altay G., Theuns T., Schaye J., Crighton N. H. M., Dalla Vecchia C., 2011, *ApJ*, 737, L37
- Barai P., Viel M., Borgani S., Tescari E., Tornatore L., Dolag K., Killedear M., Monaco P., D’Odorico V., Cristiani S., 2012, *ArXiv e-prints*
- Becker G. D., Rauch M., Sargent W. L. W., 2007, *ApJ*, 662, 72
- Bertone S., White S. D. M., 2006, *MNRAS*, 367, 247
- Bolton J. S., Haehnelt M. G., Viel M., Springel V., 2005, *MNRAS*, 357, 1178
- Bolton J. S., Oh S. P., Furlanetto S. R., 2009, *MNRAS*, 395, 736
- Bolton J. S., Viel M., Kim T.-S., Haehnelt M. G., Carswell R. F., 2008, *MNRAS*, 386, 1131
- Booth C. M., Schaye J., 2009, *MNRAS*, 398, 53
- Booth C. M., Schaye J., Delgado J. D., Dalla Vecchia C., 2012, *MNRAS*, 420, 1053
- Borgani S., Viel M., 2009, *MNRAS*, 392, L26

- Bruscoli M., Ferrara A., Marri S., Schneider R., Maselli A., Rollinde E., Aracil B., 2003, MNRAS, 343, L41
- Calura F., Tescari E., D’Odorico V., Viel M., Cristiani S., Kim T.-S., Bolton J. S., 2012, MNRAS, 422, 3019
- Cen R., Nagamine K., Ostriker J. P., 2005, ApJ, 635, 86
- Chang P., Broderick A. E., Pfrommer C., 2012, ApJ, 752, 23
- Croft R. A. C., Hu W., Davé R., 1999, Physical Review Letters, 83, 1092
- Croft R. A. C., Weinberg D. H., Bolte M., Burles S., Hernquist L., Katz N., Kirkman D., Tytler D., 2002, ApJ, 581, 20
- Croft R. A. C., Weinberg D. H., Katz N., Hernquist L., 1998, ApJ, 495, 44
- Dalla Vecchia C., Schaye J., 2008, MNRAS, 387, 1431
- Dalla Vecchia C., Schaye J., 2012, ArXiv e-prints:1203.5667
- Desjacques V., Nusser A., Sheth R. K., 2007, MNRAS, 374, 206
- Duffy A. R., Schaye J., Kay S. T., Dalla Vecchia C., Battye R. A., Booth C. M., 2010, MNRAS, 405, 2161
- Eisenstein D. J., Weinberg D. H., Agol E., Aihara H., Alende Prieto C., Anderson S. F., Arns J. A., Aubourg É., Bailey S., Balbinot E., et al. 2011, AJ, 142, 72
- Fabjan D., Borgani S., Tornatore L., Saro A., Murante G., Dolag K., 2010, MNRAS, 401, 1670
- Garzilli A., Bolton J. S., Kim T.-S., Leach S., Viel M., 2012, ArXiv e-prints: arXiv:1202.3577
- Haardt F., Madau P., 2001, in Neumann D. M., Tran J. T. V., eds, Clusters of Galaxies and the High Redshift Universe Observed in X-rays Modelling the UV/X-ray cosmic background with CUBA
- Jena T., Norman M. L., Tytler D., Kirkman D., Suzuki N., Chapman A., Melis C., Paschos P., O’Shea B., So G., Lubin D., Lin W.-C., Reimers D., Janknecht E., Fechner C., 2005, MNRAS, 361, 70
- Kawata D., Rauch M., 2007, ApJ, 663, 38
- Kennicutt Jr. R. C., 1998, ARA&A, 36, 189
- Kim T. ., Bolton J. S., Viel M., Haehnelt M. G., Carswell R. F., 2007, MNRAS, 382, 1657
- Kollmeier J. A., Miralda-Escudé J., Cen R., Ostriker J. P., 2006, ApJ, 638, 52
- Komatsu E., Smith K. M., Dunkley J., et al. 2011, ApJS, 192, 18
- Lidz A., Heitmann K., Hui L., Habib S., Rauch M., Sargent W. L. W., 2006, ApJ, 638, 27
- McCarthy I. G., Schaye J., Ponman T. J., Bower R. G., Booth C. M., Dalla Vecchia C., Crain R. A., Springel V., Theuns T., Wiersma R. P. C., 2010, MNRAS, 406, 822
- McDonald P., et al., 2006, ApJS, 163, 80
- McDonald P., Miralda-Escudé J., Rauch M., Sargent W. L. W., Barlow T. A., Cen R., Ostriker J. P., 2000, ApJ, 543, 1
- McDonald P., Seljak U., Cen R., Bode P., Ostriker J. P., 2005, MNRAS, 360, 1471
- McDonald P., Seljak U., Cen R., Shih D., Weinberg D. H., Burles S., Schneider D. P., Schlegel D. J., Bahcall N. A., Briggs J. W., Brinkmann J., Fukugita M., Ivezić Ž., Kent S., Vanden Berk D. E., 2005, ApJ, 635, 761
- McQuinn M., Lidz A., Zaldarriaga M., Hernquist L., Hopkins P. F., Dutta S., Faucher-Giguère C.-A., 2009, ApJ, 694, 842
- Meiksin A., 2000, MNRAS, 314, 566
- Meiksin A., Bryan G., Machacek M., 2001, MNRAS, 327, 296
- Meiksin A. A., 2009, Reviews of Modern Physics, 81, 1405
- Murray N., Quataert E., Thompson T. A., 2005, ApJ, 618, 569
- Oppenheimer B. D., Davé R., 2006, MNRAS, 373, 1265
- Oppenheimer B. D., Davé R., 2008, MNRAS, 387, 577
- Oppenheimer B. D., Davé R., 2009, MNRAS, 395, 1875
- Peeples M. S., Weinberg D. H., Davé R., Fardal M. A., Katz N., 2010a, MNRAS, 404, 1281
- Peeples M. S., Weinberg D. H., Davé R., Fardal M. A., Katz N., 2010b, MNRAS, 404, 1295
- Puchwein E., Pfrommer C., Springel V., Broderick A. E., Chang P., 2012, MNRAS, 423, 149
- Rauch M., 1998, ARA&A, 36, 267
- Rauch M., Miralda-Escudé J., Sargent W. L. W., Barlow T. A., Weinberg D. H., Hernquist L., Katz N., Cen R., Ostriker J. P., 1997, ApJ, 489, 7
- Schaye J., Dalla Vecchia C., 2008, MNRAS, 383, 1210
- Schaye J., Dalla Vecchia C., Booth C. M., Wiersma R. P. C., Theuns T., Haas M. R., Bertone S., Duffy A. R., McCarthy I. G., van de Voort F., 2010, MNRAS, 402, 1536
- Schaye J., Theuns T., Leonard A., Efstathiou G., 1999, MNRAS, 310, 57
- Seljak U., Makarov A., McDonald P., Trac H., 2006, Physical Review Letters, 97, 191303
- Seljak U., Slosar A., McDonald P., 2006, Journal of Cosmology and Astro-Particle Physics, 10, 14
- Semboloni E., Hoekstra H., Schaye J., van Daalen M. P., McCarthy I. G., 2011, MNRAS, 417, 2020
- Slosar A., et al., 2011, JCAP, 9, 1
- Springel V., 2005, MNRAS, 364, 1105
- Springel V., Di Matteo T., Hernquist L., 2005, MNRAS, 361, 776
- Tepper-García T., Richter P., Schaye J., Booth C. M., Dalla Vecchia C., Theuns T., 2012, ArXiv e-prints:1201.5641
- Tescari E., Viel M., D’Odorico V., Cristiani S., Calura F., Borgani S., Tornatore L., 2011, MNRAS, 411, 826
- Tescari E., Viel M., Tornatore L., Borgani S., 2009, MNRAS, 397, 411
- Theuns T., Bernardi M., Frieman J., Hewett P., Schaye J., Sheth R. K., Subbarao M., 2002, ApJ, 574, L111
- Theuns T., Schaye J., Haehnelt M. G., 2000, MNRAS, 315, 600
- Theuns T., Schaye J., Zaroubi S., Kim T.-S., Tzanavaris P., Carswell B., 2002, ApJ, 567, L103
- Theuns T., Viel M., Kay S., Schaye J., Carswell R. F., Tzanavaris P., 2002, ApJ, 578, L5
- Tornatore L., Borgani S., Viel M., Springel V., 2010, MNRAS, 402, 1911
- Tytler D., Kirkman D., O’Meara J. M., Suzuki N., Orin A., Lubin D., Paschos P., Jena T., Lin W.-C., Norman M. L., Meiksin A., 2004, ApJ, 617, 1
- van Daalen M. P., Schaye J., Booth C. M., Dalla Vecchia C., 2011, MNRAS, 415, 3649
- Vernet J., et al., 2011, A&A, 536, A105
- Viel M., Becker G. D., Bolton J. S., Haehnelt M. G., Rauch M., Sargent W. L. W., 2008, Physical Review Letters, 100, 041304
- Viel M., Bolton J. S., Haehnelt M. G., 2009, MNRAS, 399, L39

- Viel M., Branchini E., Dolag K., Grossi M., Matarrese S., Moscardini L., 2009, MNRAS, 393, 774
- Viel M., Haehnelt M. G., 2006, MNRAS, 365, 231
- Viel M., Haehnelt M. G., Springel V., 2004, MNRAS, 354, 684
- Viel M., Haehnelt M. G., Springel V., 2010, JCAP, 6, 15
- Viel M., Marković K., Baldi M., Weller J., 2012, MNRAS, p. 2448
- Wiersma R. P. C., Schaye J., Smith B. D., 2009, MNRAS, 393, 99
- Wiersma R. P. C., Schaye J., Theuns T., 2011, MNRAS, 415, 353
- Wiersma R. P. C., Schaye J., Theuns T., Dalla Vecchia C., Tornatore L., 2009, MNRAS, 399, 574
- Zaroubi S., Viel M., Nusser A., Haehnelt M., Kim T.-S., 2006, MNRAS, 369, 734

## APPENDIX A: BOX-SIZE AND RESOLUTION EFFECTS

In this appendix, we consider box-size and resolution effects for the reference (*REF*) runs. In Figure A1, we quantify the effects that a different box size has on the flux PDF (left panel) and on the flux power (right panel) by considering three different boxes of linear comoving size 100, 50 and 25  $h^{-1}$  Mpc at fixed resolution and at  $z = 2.25$ . From the Figure we conclude that the 50 and 100  $h^{-1}$  Mpc boxes agree well for  $k \geq 1h/\text{Mpc}$ . The fact that large scale modes are affected is not surprising, but this issue is not critical for us since we are interested in the differences of various physical models relative to the reference model run *in the same box size from the same initial conditions*.

Figure A2 quantifies resolution effects by comparing two reference runs: the (25,256), represented by the continuous red curve, and the (25,128), represented by the dot-dashed red curve, to the reference run at higher resolution (25,512). Note that the mass (spatial) resolution varies by factors of 8 (2) between each pair of simulations. At  $z = 2.25$  the flux PDF is converged to better than 5% over the whole flux range and the flux power is also converged at the 3% level up to  $k = 3h/\text{Mpc}$  between the (25,256) and (25,512) runs. At higher redshifts,  $z = 3, 4$  (dashed, orange and dotted, green curves, respectively) we compare the (25,256) and the (25,512) simulations and find that the convergence is worse. We believe that numerical errors induced by poor resolution are likely to be smaller than the values quoted above when the (25,512) simulations are considered (we would require a higher resolution simulation to confirm this). The fact that we are interested in relative differences between different models using *the same resolution* will largely mitigate any resolution effects. An exception may be the importance of feedback from low-mass galaxies, which we will underestimate if the star formation rate in low-mass haloes is limited by the finite resolution. This may be the case at higher redshifts.

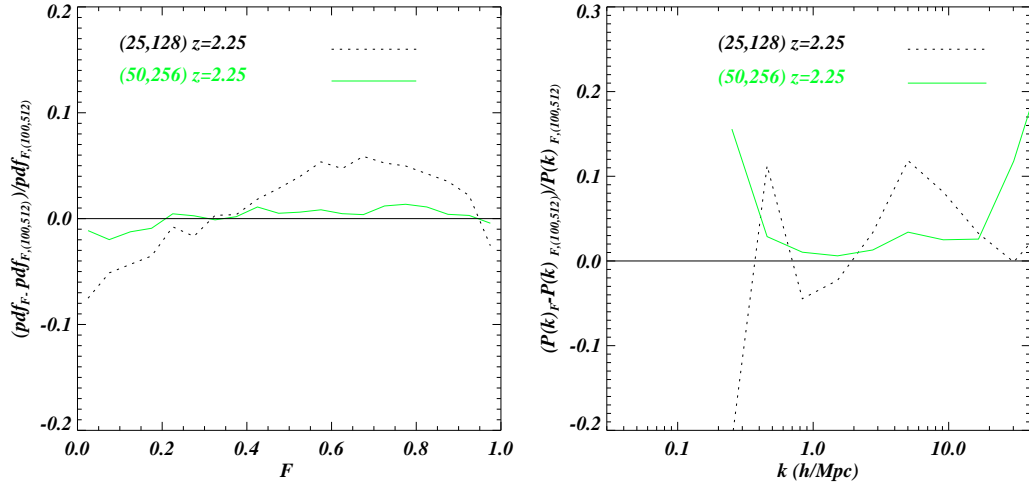


**Figure A1.** Effect of different box size at fixed resolution for the *REF* simulations at  $z = 2.25$ . We plot the difference of the (25,128) (black, dotted) and (50,256) (green, solid) boxes relative to the (100,512) simulation, respectively (the flux power results are only shown for the range of wavenumbers in which there is overlap between the different boxes).

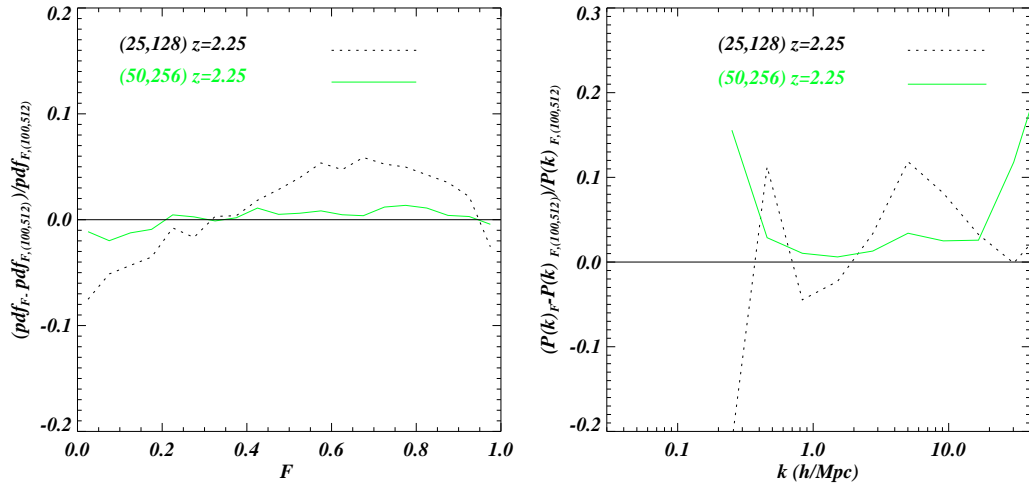


**Figure A2.** Effect of numerical resolution for the reference (*REF*) simulations at  $z = 2.25, 3, 4$ . We plot the relative difference of the (25,256) and the (25,512) simulation as the red solid ( $z = 2.25$ ), dashed orange ( $z = 3$ ) and green dotted curves ( $z = 4$ ). We also show the ratio of the (25,128) and (25,512) boxes at  $z = 2.25$  as a red dot-dashed curve.